

Understanding Future Change of Global Monsoons Projected by CMIP6 Models

BIN WANG

Department of Atmospheric Sciences, University of Hawai'i at Mānoa, Honolulu, Hawaii, and Earth System Modeling Center, Nanjing University of Information Science and Technology, Nanjing, China

CHUNHAN JIN

Key Laboratory for Virtual Geographic Environment, Ministry of Education, and State Key Laboratory Cultivation Base of Geographical Environment Evolution of Jiangsu Province, and Jiangsu Center for Collaborative Innovation in Geographical Information Resource Development and Application, and School of Geography Science, Nanjing Normal University, Nanjing, China

JIAN LIU

Key Laboratory for Virtual Geographic Environment, Ministry of Education, and State Key Laboratory Cultivation Base of Geographical Environment Evolution of Jiangsu Province, and Jiangsu Center for Collaborative Innovation in Geographical Information Resource Development and Application, and School of Geography Science, Nanjing Normal University, and Jiangsu Provincial Key Laboratory for Numerical Simulation of Large Scale Complex Systems, School of Mathematical Science, Nanjing Normal University, Nanjing, China

(Manuscript received 26 December 2019, in final form 7 May 2020)

ABSTRACT


Projecting future change of monsoon rainfall is essential for water resource management, food security, disaster mitigation, and infrastructure planning. Here we assess the future change and explore the causes of the changes using 15 models that participated in phase 6 of the Coupled Model Intercomparison Project (CMIP6). The multimodel ensemble projects that, under the shared socioeconomic pathway (SSP) 2–4.5, the total land monsoon rainfall will likely increase in the Northern Hemisphere (NH) by about 2.8% per one degree Celsius of global warming ($2.8\% \text{ }^{\circ}\text{C}^{-1}$) in contrast to little change in the Southern Hemisphere (SH; $-0.3\% \text{ }^{\circ}\text{C}^{-1}$). In addition, in the future the Asian–northern African monsoon likely becomes wetter while the North American monsoon becomes drier. Since the humidity increase is nearly uniform in all summer monsoon regions, the dynamic processes must play a fundamental role in shaping the spatial patterns of the global monsoon changes. Greenhouse gas (GHG) radiative forcing induces a “NH-warmer-than-SH” pattern, which favors increasing the NH monsoon rainfall and prolonging the NH monsoon rainy season while reducing the SH monsoon rainfall and shortening the SH monsoon rainy season. The GHG forcing induces a “land-warmer-than-ocean” pattern, which enhances Asian monsoon low pressure and increases Asian and northern African monsoon rainfall, and an El Niño–like warming, which reduces North American monsoon rainfall. The uncertainties in the projected monsoon precipitation changes are significantly related to the models’ projected hemispheric and land–ocean thermal contrasts as well as to the eastern Pacific Ocean warming. The CMIP6 models’ common biases and the processes by which convective heating drives monsoon circulation are also discussed.

1. Introduction

Land monsoon rainfall (LMR) provides water resources for about two-thirds of today’s world population. Projecting future change of global monsoon

(GM) rainfall and understanding its underlying physics is fundamentally crucial for infrastructure planning, food security, disaster mitigation, and water resource management.

Despite hundreds of years of research, the definition and geographic domains of monsoons continue to evolve. Monsoon climate is characterized by both annual reversals of surface winds and contrast between rainy summer and dry winter (Webster 1987). The classical delineation of the monsoon regime, however,

 Denotes content that is immediately available upon publication as open access.

Corresponding author: Jian Liu, jliu@njnu.edu.cn

DOI: 10.1175/JCLI-D-19-0993.1

© 2020 American Meteorological Society. For information regarding reuse of this content and general copyright information, consult the [AMS Copyright Policy](https://www.ametsoc.org/PUBSReuseLicenses) (www.ametsoc.org/PUBSReuseLicenses).

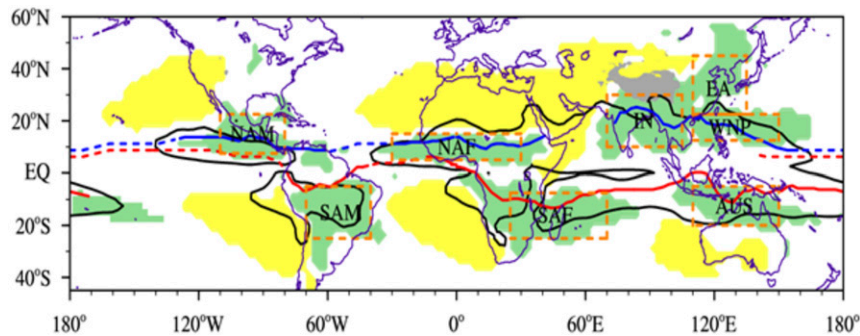


FIG. 1. The monsoon precipitation domains (green shading) defined by the regions where local summer-minus-winter precipitation exceeds 300 mm and the local summer precipitation exceeds 55% of the annual total. The monsoon westerly domains (black lines) are defined by the monsoon westerly index (MWI) > 0.5 . Here the MWI = AR/AM of the 850-hPa zonal winds, where AR denotes the annual range between local summer westerly and winter easterly components, and AM measures the annual mean zonal wind speed. The area where MWI is greater than 0.5 outlines the tropical monsoon domain (Wang and Ding 2008). Summer denotes May–September for the NH and November–March for the SH. The dry regions (yellow shading) are regions where the local summer precipitation is less than 150 mm. The blue lines indicate the ITCZ position in August, and the red lines indicate the maximum monthly mean precipitation in February; solid lines denote monsoon troughs, and dashed lines show the trade wind convergence. This figure is modified from P. X. Wang et al. (2017).

was based solely on the annual reversal of surface winds (Hann 1908; Khromov 1957; Ramage 1971), and the resultant monsoons are primarily confined to the tropical Eastern Hemisphere. Considering the socioeconomic and scientific importance of monsoon rainfall, the modern definition of monsoon is based on rainfall characteristics, and the resultant monsoon domain extends to include the North and South American monsoons, as well as the southern African monsoon (Wang 1994; Wang and Ding 2006).

Figure 1 illustrates the monsoon rain domains defined by two simple criteria in rainfall characteristics (green shading) along with the tropical monsoon domain defined by an annual reversal of zonal winds (black curves). Note that the westerly monsoon domains are generally situated on the equatorward and western sides of the monsoonal rainfall domain due to dispersion of the Rossby waves generated by monsoon precipitation heating. Thus, the two definitions are dynamically consistent except that the subtropical East Asian monsoon features an annual reversal of meridional winds. In this study, we used the rainfall domain, which includes northern and southern African, North and South American, South Asian, East Asian, and Australian monsoon regions, as well as the western North Pacific monsoon. The North American monsoon domain in some literature refers only to western Mexico and Arizona, but here we broaden it to a large-scale North American monsoon domain, including Central America

and Venezuela. Note also that the monsoon precipitation domain reflects large-scale features. Over the Maritime Continent, the definition of the monsoon rainy season is complicated because the rainfall is a strong function of the interaction of seasonally reversed winds and the mesoscale terrain (Chang et al. 2005, 2016), so over Borneo, for instance, the rainy season is in northern winter, and it was not marked in the monsoon domain.

Physically, the GM is a forced response of the coupled climate system to annual variation of solar insolation, and it represents the leading mode of annual variations of global tropical and subtropical rainfall and circulation (Wang and Ding 2008; Wang et al. 2014). The GM system can be defined as a planetary-scale circulation system with a seasonal reversal of the three-dimensional monsoon circulation that is accompanied by meridional migration of the monsoon convergence zone. This statement is an expanded view of the global overturning circulation visualized by Trenberth et al. (2000).

Understanding how the GM precipitation may change in the future is of central importance for understanding climate change. GM precipitation plays pivotal roles in driving atmospheric general circulation through releasing latent heat and is fundamental to the global water and energy cycle. During June–September (JJAS), about 70% of the tropical precipitation falls in the NH summer monsoon region. The latent heat released in the

heavy monsoon rains lifts air upward, forming a global-scale overturning circulation. The meridional branches of divergent monsoon flows form the backbone of the Hadley circulation. About three-quarters of the inter-tropical convergence zone (ITCZ) is embedded within the monsoon regions (Fig. 1), which determines the annual migration of the ITCZ. Global desert regions are generally located to the western and poleward side of the summer monsoons (Fig. 1) due to the descent resulting from the interaction between monsoon heating-induced Rossby waves and the mean westerly flow on their poleward side (Hoskins 1996; Rodwell and Hoskins 1996; Hoskins and Wang 2006). The GM not only governs the flow of water and energy within the climate system but also plays a crucial role in determining the climate system's albedo and emission of longwave radiation to space (P. X. Wang et al. 2017).

The Intergovernmental Panel on Climate Change (IPCC) Fifth Assessment Report (AR5) indicates that the GM area, intensity, and precipitation (GMP) are either likely or very likely to increase by the end of the twenty-first century (Hsu et al. 2013; Christensen et al. 2013). The GM change is dominated by increases in the NH (Kitoh et al. 2013). Earlier or unchanged onset dates and a later retreat makes the GM season likely to increase in length (Christensen et al. 2013; Lee and Wang 2014). Lee and Wang (2014) demonstrated a near-linear scaling of GMP with global mean temperature as the twenty-first century progresses, with a stronger signal in the NH related to the temperature difference between the NH and SH. However, the fundamental drivers for the complex pattern of GM precipitation change have not been fully understood.

Our objective is to use CMIP6 CGCMs (Eyring et al. 2016) to assess future changes of the monsoon from a global perspective and to identify the key drivers for the global monsoon changes. Specifically, we aim to find out the common biases of the models, and the physical reasoning that supports the models' projected changes. A detailed description of the models and data used is given in section 2. Section 3 evaluates historical simulations against the observation for the period of 1979–2014. Section 4 assesses future changes of GMP. Section 5 elaborates the physics behind the change. A summary and discussion are presented in the last section.

2. Observational datasets and CMIP6 model results

The pentad and monthly precipitation data used in this study are from the Global Precipitation Climatology Project (GPCP), version 2.3 (v2.3; Adler et al. 2003). For the monthly mean sea surface temperature (SST), we

used the arithmetic mean of two datasets: the Hadley Centre Sea Ice and Sea Surface Temperature (HadISST) (Rayner et al. 2003) and the National Oceanic and Atmospheric Administration Extended Reconstructed SST (ERSST), version 5 (Huang et al. 2017) for the reasons discussed in Wang et al. (2019). All datasets cover the period 1979–2014.

We have examined 24 CMIP6 models (Table 1). However, the results presented here are based on analysis of 15 early-released models (Table 1). When the other nine models' results became available, we conducted a parallel analysis with the 24 models. Comparison of the 24 models' MME and 15 models' MME results indicates that the differences between them are generally negligible and the conclusions derived from 15 MME are robust.

To evaluate models' performance and to lay a baseline for assessing future changes, we used the historical runs for the period 1979–2014 to determine the present-day climate. To assess future climate, we analyze the data for the period of 2065–2100 derived from the climate projections under the Shared Socioeconomic Pathway 2–4.5 (SSP2–4.5) in the CMIP6 archive. Future climate change is determined by the difference in climatology between the present-day (1979–2014) and future (2065–2100) climatology. The SSP2–4.5 scenario is an updated version of the representative concentration pathway 4.5 (RCP4.5) of CMIP5, assuming the same medium level of greenhouse gas emission scenario and assuming the radiative forcing will stabilize at about 4.5 W m^{-2} after 2100. The land use and aerosol pathways specified in SSP2–4.5 are combined with an intermediate level of societal vulnerability (O'Neill et al. 2016). For a fair comparison, all data are interpolated to a standard grid of $2.5^\circ \times 2.5^\circ$, except for the monthly precipitation, which has a resolution of $1.0^\circ \times 1.0^\circ$.

3. CMIP6 models' performance and common biases

The solstice seasonal mean conditions describe the dominant mode of the annual cycle of the global monsoon. Figure 2 (top and middle panels) shows that the 15 models' multimodel ensemble mean (15MME for short) captures observed boreal summer (JJAS) climatology very well with a pattern correlation coefficient (PCC) = 0.92 and a relatively small normalized root-mean-square error (NRMSE) of 0.44. The performance is better than that of the MME of CMIP5's four best models (B4MME; the models are CanESM2, CNRM-CM5, HadGEM2-ES, and MIROC5; NRMSE = 0.48). However, the models have significant common biases in

TABLE 1. Description of CMIP6 models used in the study. An asterisk indicates the 15 early-released CMIP6 models [expansions of most model acronyms are available online (<https://www.ametsoc.org/PubsAcronymList>)].

Model acronym	Institution	Atmosphere resolution (lat. \times lon)
ACCESS-ESM1.5	Australian Community Climate and Earth System Simulator (ACCESS)	145 \times 192
*BCC_CSM2-MR	Beijing Climate Center, China Meteorological Administration (BCC)	160 \times 320
*CanESM5	Canadian Centre for Climate Modeling and Analysis (CCCma)	64 \times 128
*CESM2	National Center for Atmospheric Research (NCAR)	192 \times 288
*CESM2(WACCM)		192 \times 288
*CNRM-CM6.1	Centre National de Recherches Meteorologiques/Centre	128 \times 256
*CNRM-ESM2.1	Europeen de Recherche et Formation Avancees en Calcul Scientifique (CNRM/CERFACS)	128 \times 256
*EC-EARTH3-Veg	European Consortium (EC)	256 \times 512
FGOALS-g3	Chinese Academy of Sciences (CAS)	80 \times 180
FIO-ESM-2.0	First Institute of Oceanography, Ministry of Natural Resources (FIO)	192 \times 288
*GFDL CM4	Geophysical Fluid Dynamics Laboratory (NOAA GFDL)	180 \times 288
GFDL-ESM4		180 \times 288
*HadGEM3-GC31-LL	Met Office Hadley Centre (MOHC)	144 \times 192
INM-CM5.0	Institute of Numerical Mathematics of the Russian Academy of Sciences	120 \times 180
*IPSL-CM6A-LR	Institute Pierre-Simon Laplace (IPSL)	143 \times 144
KACE-1.0-G	National Institute of Meteorological Sciences/Korea Meteorological Administration (NIMS-KMA)	144 \times 192
MCM-UA-1.0	The University of Arizona (UA)	80 \times 96
*MIROC6	Atmosphere and Ocean Research Institute (University of Tokyo), National Institute for Environmental Studies, and Japan Agency for Marine-Earth Science and Technology (MIROC)	128 \times 256
*MIROC-ES2L		64 \times 128
MPI-ESM1.2-HR	Max Planck Institute for Meteorology (MPI-M)	192 \times 384
*MRI-ESM2.0	Meteorological Research Institute (MRI)	160 \times 320
*NESM3	Nanjing University of Information Science and Technology (NUIST)	96 \times 192
NorESM2-MM	Bjerknes Centre for Climate Research (BCCR)	192 \times 288
*UKESM1.0-LL	Natural Environment Research Council and the Met Office Hadley Centre	144 \times 192

the equatorial regions between 15°S and 15°N. In the Pacific Ocean, deficient rainfall is seen along the equator while excessive rainfall to its adjacent poleward sides. Over the Indian Ocean, wet and dry biases are seen to the north and south of the equator, respectively. The equatorial Atlantic Ocean is dominated by a wet bias. These biases link to the dry biases in the NH land monsoon regions and wet biases in NH oceanic monsoon regions. The southern summer [December–March (DJFM)] simulation skill is slightly lower than those for the JJAS season (PCC = 0.90, NRMSE = 0.52) but still improved compared to CMIP5 B4MME (NRMSE = 0.54). The major bias pattern in the Pacific resembles that in JJAS with a prominent double ITCZ. Other wet biases are seen over the western equatorial Indian Ocean, “Maritime Continent,” and equatorial South Atlantic. These wet biases result in wet biases in SH monsoon regions, including southern Africa, Indonesia, and eastern Brazil.

The simulated GMP domain and intensity are evaluated in the bottom panels of Fig. 2. The GMP intensity is defined by the ratio of local summer-minus-winter precipitation to the annual total, which measures the degree of “wet summer–dry winter” contrast or monsoon-like seasonality. The GMP intensity is generally very well simulated by the MME with PCC = 0.90 and NRMSE = 0.45, which is slightly better than the CMIP5 counterpart (NRMSE = 0.48). The models tend to underestimate GMP intensity in the East Asian and Mexican monsoon regions, while overestimating it in subtropical dry regions, including the Sahara, Arabia, the southeast Pacific, and the South Atlantic. Monsoon domains are generally realistically simulated over land, but the simulated oceanic monsoon domains extend too far into the middle of oceans. The skill in the simulated GMP domain is about the same as in the CMIP5 models’ MME. In this paper, the observed monsoon domain has been used to make analyses of the monsoon rainy season,

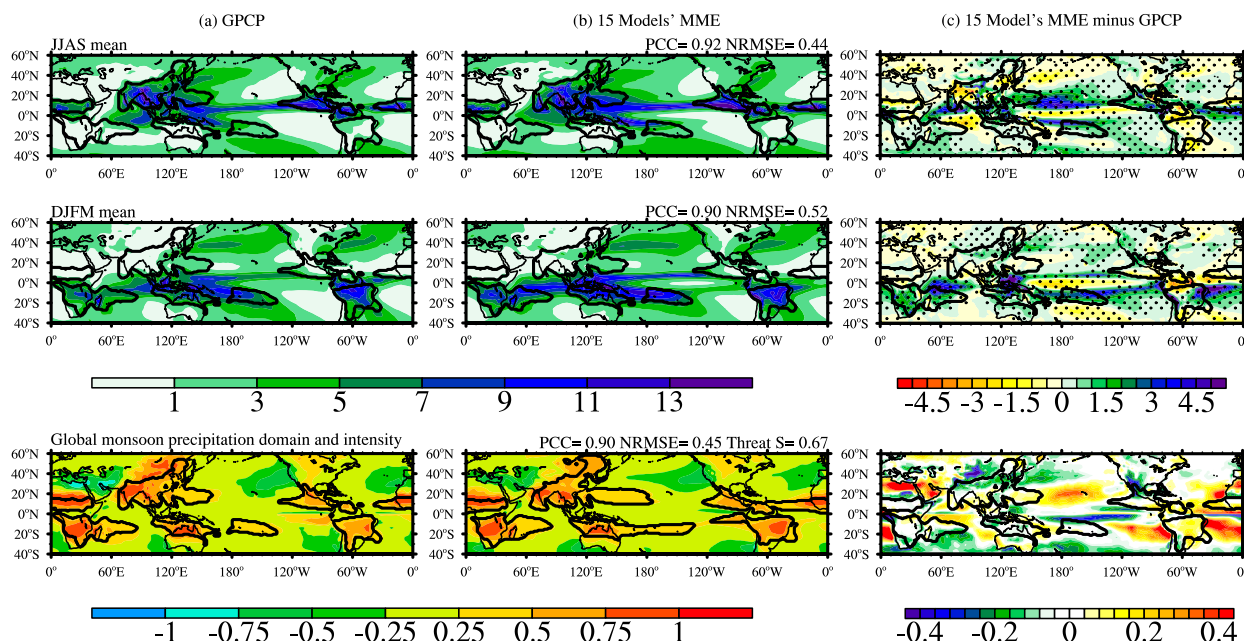


FIG. 2. Comparison of the precipitation climatology (1979–2014) derived from (a) observations, (b) 15 models' MME simulation, and (c) the MME biases, for (top) JJAS mean precipitation rate, (middle) DJFM mean precipitation rate, and (bottom) global monsoon domain and intensity.

interannual variability of GMP, and the monsoon rainfall change.

To present an integrated view of the response of the NH and SH monsoon precipitation to solar radiative forcing during the year, we examine hemispheric-scale monsoon onset, peak, and withdrawal. This integrated hemispheric view is a useful measure of the rainy season, even though the rainy season varies significantly from region to region (Zhang and Wang 2008). Figures 3a and 3b and Table 2 indicate that the observed NH monsoon (NHM; including both land and ocean) area-weighted mean precipitation rate ranges from 0.99 mm day^{-1} in pentad 6 (26–30 January) to 8.33 mm day^{-1} at pentad 43 (30 July–3 August) with an annual mean rate of 4.05 mm day^{-1} . The onset of the NH summer monsoon measured by the time when the mean precipitation increases from below to above 5 mm day^{-1} is around pentad 29 (21–25 May). The withdrawal of the NH summer monsoon measured by the time when the mean precipitation decreases from above to below 5 mm day^{-1} is around pentad 57 (8–12 October). So, roughly speaking, the NH monsoon rainy season is from late May to mid-October, lasting for about five months. The observed SH monsoon (SHM) area-weighted mean precipitation rate ranges from 0.90 mm day^{-1} at pentad 45 (9–13 August) to about 7.12 mm day^{-1} at pentad 7 (31 January–4 February) with an annual mean rate of 3.56 mm day^{-1} . The onset of the SH summer

monsoon is around pentad 68 (2–6 December). The withdrawal of the SH summer monsoon is around pentad 18 (27–31 March). The SH monsoon rainy season is approximately from early December to late March, lasting about four months, shorter than the NH counterpart.

Among the 15 models, only 11 models provided pentad precipitation data. The CMIP6 11 models' MME simulated seasonal cycle is more accurate in NHM than the SHM. More specifically, the simulated NH mean monsoon precipitation is only 1.7% higher than the observed. Although precipitation is overproduced from July to November, the bias in the maximum precipitation is only about 0.20 mm day^{-1} (about 2.4% higher). The simulated onset and withdrawal dates are delayed by 2 and 1 pentad, respectively. On the other hand, the annual mean precipitation in SHM regions is overproduced (4.28 mm day^{-1}) by about 20.2%. The overestimated precipitation occurs from November to the next July, with the maximum bias up to 18.4% in March. The simulated onset is advanced by two pentads, while the withdrawal date is markedly delayed by 4.5 pentads (Table 2). The delayed withdrawal bias of 4.5 pentad arises from the models' overestimated rainfall during local summer and fall. This bias occurs primarily over the oceanic monsoon region of southern Africa.

We are specifically concerned with the simulated land monsoon precipitation, which is shown in Figs. 3c and 3d

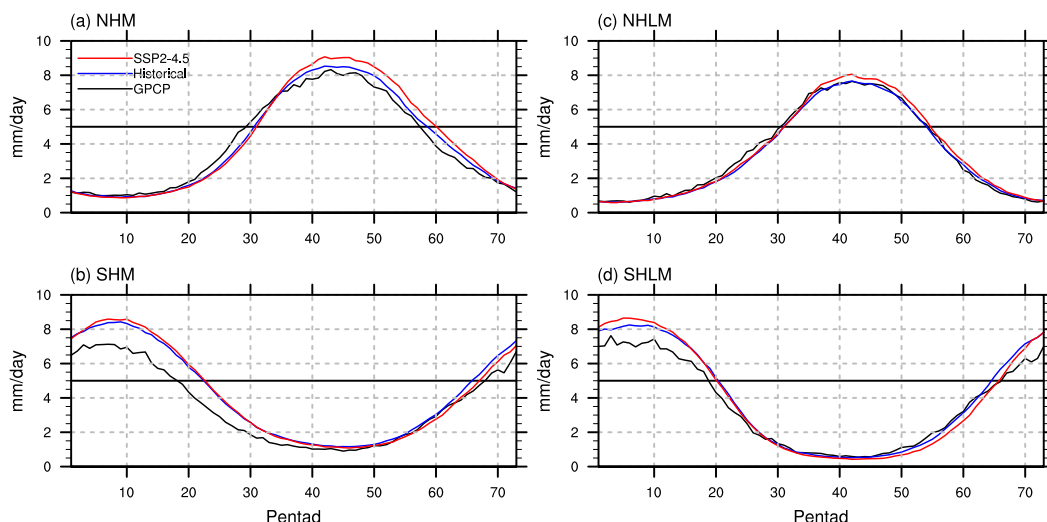


FIG. 3. Comparison of annual cycles (pentad climatology) of the total (both land and ocean) monsoon precipitation averaged in the (a) NH and (b) SH. (c),(d) As in (a) and (b), but for the NH and SH land-only monsoon precipitation, respectively. The black, blue, and red curves represent, respectively, the observations (1979–2014), the 11 models' MME historical simulation (1979–2014), and CMIP6 SSP2–4.5 projection (2065–2100). The onset and withdrawal dates are defined as the Julian pentad for which the pentad mean precipitation rate starts to be respectively above and below 5 mm day^{-1} (black horizontal line). Models used here include BCC_CSM2, CanESM5, CESM2, CESM2(WACCM), CNRM-CM6.1, CNRM-ESM2.1, GFDL CM4, EC-EARTH3-Veg, IPSL-CM6A-LR, NESM, and MRI-ESM2.0.

and Table 3. The simulated land monsoon rainy season is better than those of the total monsoon rainfall. The 11 models' MME simulated realistic annual mean precipitation in the NH land monsoon region (3.42 mm day^{-1}), which is underestimated by about 2.3%; but in the SH land monsoon region, the mean precipitation rate (3.91 mm day^{-1}) is overproduced by 9.5%. The overestimated SH land monsoon precipitation occurs from November to next April, with the maximum precipitation rate of about 8.3% higher. The simulated onset (withdrawal) date in the NH land monsoon is accurate: The onset at pentad 30–31 (end of May and beginning of June) and withdrawal on pentad 54 (end of September), lasting about four months, primarily in JJAS. The onset and withdrawal dates of the NH summer monsoon

obtained by using the criterion 5 mm day^{-1} match the Indian monsoon onset and withdrawal dates very well (Joseph et al. 2006; Wang et al. 2009). In the SH, the observed land monsoon onset is at pentad 66 (22–26 November) and withdrawal at pentad 18.5 (29 March–2 April), also lasting about four months, primarily covering DJFM. The simulated onset is earlier by 5–10 days, but the withdrawal delayed by 5–10 days. Overall, the biases are considerably small over land compared with that over oceans.

Another aspect of evaluation is the interannual variability of GMP and its relationship with El Niño–Southern Oscillation (ENSO). Figure 4a shows the spatial pattern of the leading empirical orthogonal function (EOF) mode of the monsoon year GMP. The

TABLE 2. Characteristic quantities in the annual cycle (pentad climatology) of the total NHM and SHM precipitation. The unit for rainfall is millimeters for day, and the unit for onset and withdrawal is Julian pentad. In the minimum (Min) and maximum (Max) columns, the first value is precipitation (mm day^{-1}) and the value in parentheses is the corresponding pentad.

		Min	Mean	Max	Onset	Withdrawal
NHM	Observation	0.99 (6)	4.05	8.33 (43)	29	57
	Historical	0.90 (9)	4.12	8.53 (42)	31	58
	SSP2–4.5	0.87 (9)	4.30	9.07 (42)	31	60
SHM	Observation	0.90 (45)	3.56	7.12 (7)	68	18
	Historical	1.16 (44)	4.28	8.43 (9)	66	22.5
	SSP2–4.5	1.08 (46)	4.23	8.59 (7)	67	22.5

TABLE 3. As in Table 2, but for the NH and SH land monsoon precipitation.

		Min	Mean	Max	Onset	Withdrawal
NH land monsoon	Observation	0.61 (6)	3.50	7.64 (42)	30.5	54
	Historical	0.61 (4)	3.42	7.66 (42)	31	54
	SSP2-4.5	0.58 (3)	3.57	8.06 (42)	31	54.5
SH land monsoon	Observation	0.55 (43)	3.57	7.62 (3)	66	18.5
	Historical	0.52 (42)	3.91	8.25 (6)	64.5	20
	SSP2-4.5	0.42 (42)	3.83	8.65 (5)	66	20

monsoon year starts from May and lasts to the next April (Yasunari 1991), which coincides with a typical life cycle of an El Niño event from onset to decay (B. Wang et al. 2017). The 15 models' averaged EOF1 captures realistic spatial patterns of the observed leading mode of interannual variability of the GMP (PCC = 0.83) (Fig. 4a). The observed leading mode is simultaneously correlated with the Niño-3.4 index with a correlation coefficient (CC) of -0.91 ($n = 34$; $p < 0.01$), and the simulated leading mode has a CC with the Niño-3.4 index of -0.64 ($n = 31$; $p < 0.01$), suggesting that the MME reproduces reasonably well the interannual variability of the GMP but significantly underestimates its relationship with ENSO.

Figure 4b shows the observed global precipitation anomalies during a monsoon year associated with the simultaneous Niño-3.4 index. The observed pattern exhibits a global-scale, zonal wavenumber-2 pattern.

Over the equator, an El Niño causes increased rainfall over the western Pacific and the western Indian Ocean but decreased rainfall over the Maritime Continent and tropical South America and Atlantic. The equatorial rainfall anomalies emanate to the midlatitudes, forming poleward and eastward precipitation belts. The 15MME replicates well the correlation patterns (PCC = 0.82), but the correlation coefficients are reduced in nearly all monsoon regions, consistent with the conclusions derived from Fig. 4a.

4. Assessment of projected future changes of global monsoon

a. Annual cycles and rainy season of the total monsoon precipitation

The total monsoon precipitation includes all precipitation falling over both the land and ocean monsoon

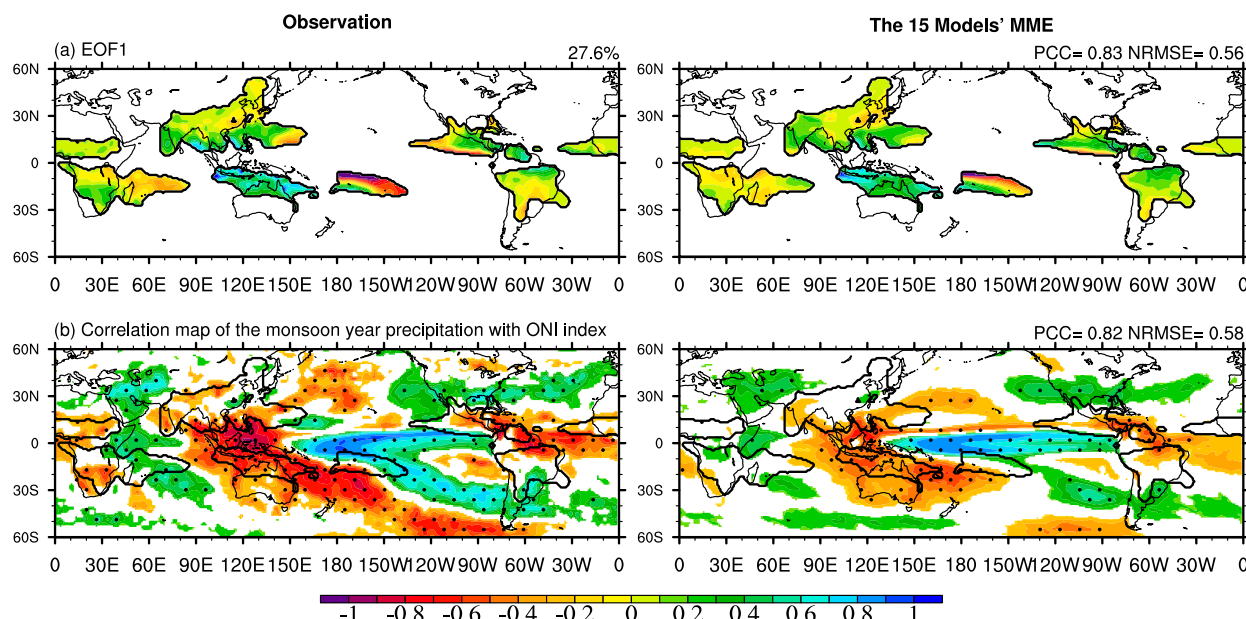


FIG. 4. Comparison of the global monsoon interannual variability (1979–2014) between (left) the observation and (right) simulation in the CMIP6 historical run by 15 models' MME, showing (a) spatial patterns of the leading EOF modes of the monsoon year (from May to next April) precipitation anomalies in the GM domain and (b) the correlation map of the monsoon year mean precipitation with reference to the simultaneous ONI index (SSTA averaged over Niño-3.4 region).

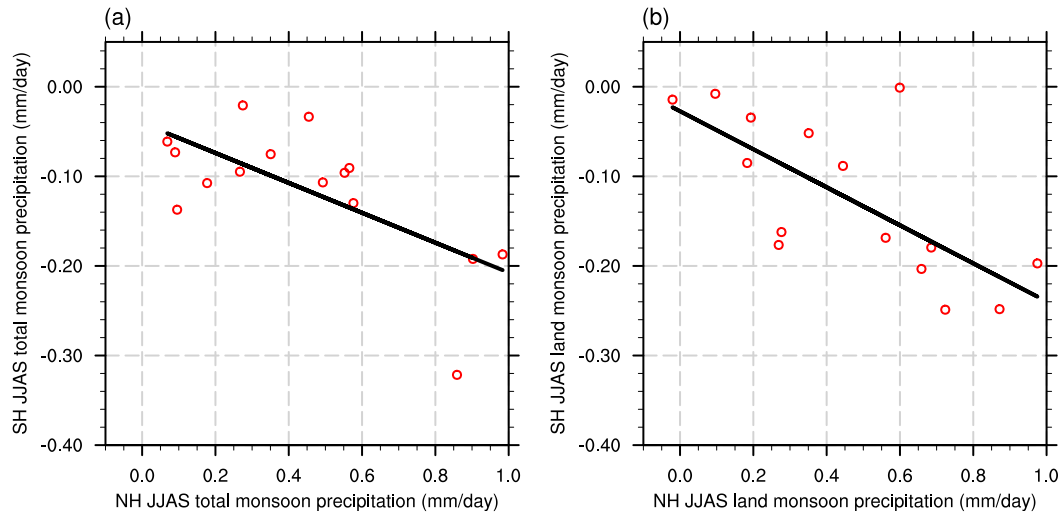


FIG. 5. Scatter diagram showing the linkage between SH summer monsoon and NH winter monsoon precipitation derived from the 15 CMIP6 models: (a) SH JJAS total monsoon precipitation as a function of the NH JJAS total monsoon precipitation and (b) SH JJAS land monsoon precipitation as a function of the NH JJAS land monsoon precipitation. The correlation coefficients are -0.67 ($p < 0.01$) in (a) and -0.71 ($p < 0.01$) in (b).

regions. The total monsoon rainfall reflects the overall response of the hemispheric monsoon to GHG forcing. The projected changes in the annual range, onset, peak, and withdrawal pentads for the hemispheric mean precipitation are shown in Table 2. The annual range is measured by the maximum and minimum pentad rainfall. The projected annual range of the NHM as a whole increase by 7.5% (from 7.63 to 8.20 mm day⁻¹), which is primarily due to increased summer maximum precipitation (6.3%). On the other hand, the annual range in the SHM increases only by 3.3% from 7.27 to 7.51 mm day⁻¹, which is contributed by both increased summer maximum (1.9%) and decreased winter minimum rainfall (-6.9%). The pronounced decreased winter precipitation in the SHM is arguably a result of enhanced NH summer monsoon precipitation-induced subsidence through meridional circulations, which overrides the opposing effects of increased specific humidity and land–sea thermal contrast. To support this hypothesis, we examined the intermodal spread. Results show that models with more suppressed SH winter monsoon precipitation correlate significantly with more intense NH summer monsoon precipitation in both the land monsoon region and the entire (both land and ocean) monsoon region (Fig. 5). Figure 5 suggests an intrinsic linkage between NH and SH monsoons through meridional circulation. The amplification of monsoonal annual range implies that in monsoon regions, the wet season gets wetter and the dry season gets drier, confirming the results of Zhang et al. (2019). This change

will increase the chances of summer floods and winter dryness.

The projected onset of the NH summer monsoon in CMIP6 shows no change in the onset, but the withdrawal delays by about 10 days so that the NH summer monsoon rainy season lengthens by about 10 days (Table 2). Both the projected onset and peak dates in the SHM delay by about 5 days, while the withdrawal date does not change appreciably. The projected insignificant change in the onset and withdrawal dates is consistent with the insignificant change of the projected total amount and annual range of the SHM precipitation (Fig. 3b). The conclusion here is different from the CMIP5 assessment of Lee and Wang (2014), which concluded that the NH monsoon onset would be advanced based on the projected increase in May precipitation, but is more consistent with the results of Kitoh et al. (2013), who used different methods and suggested a lengthening of the global monsoon season, which is mainly attributed to the delayed retreat dates, while the projected onset dates either advance or show no change.

b. Annual cycles and rainy season of the land monsoon precipitation

The changes in land monsoon rainfall are different from those over oceanic monsoon regions. Therefore, we will focus on LMR changes (Table 3). The projected annual range of NH LMR increases by 6.1% from 7.05 to 7.48 mm day⁻¹, which is due to increased summer

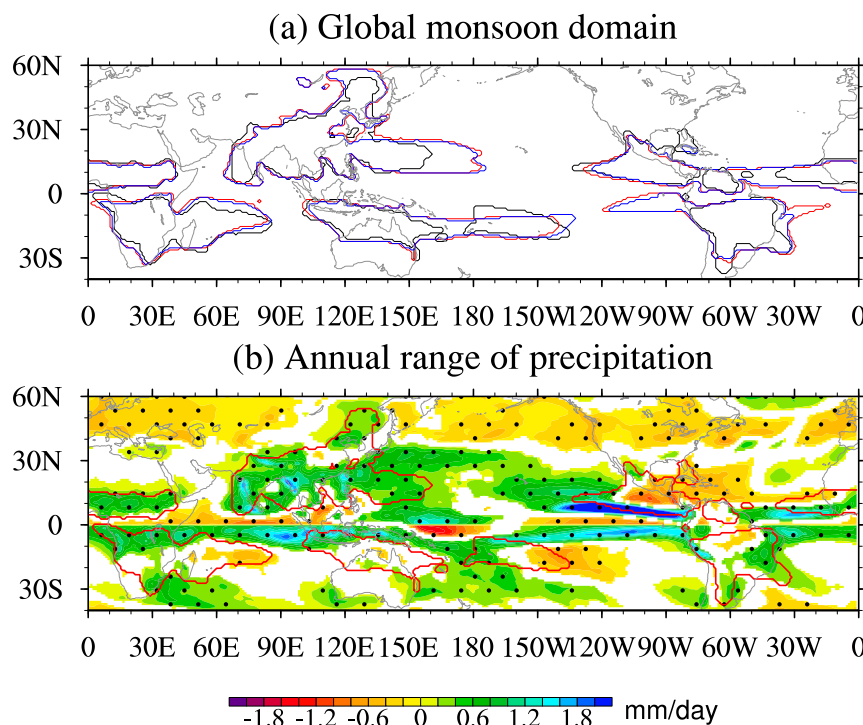


FIG. 6. Future change of GM properties (2065–2100 relative to 1979–2014): (a) Change of the GM domain. The black, blue, and red lines represent, respectively, the observations, the 15 models' MME historical simulation, and the SSP2–4.5 projection. (b) Changes in the annual range of precipitation. The color-shaded areas are significant at the 66% confidence level; the stippled areas are significant at the 95% confidence level using a two-tailed Student's t test.

maximum rainfall (5.2%) and decreased winter minimum (4.9%). The counterpart of SH LMR increases by 6.5% from 7.73 to 8.23 mm day^{−1}, which is considerably larger than that over ocean monsoon regions and is contributed by increased summer maximum (4.8%) and decreased winter minimum (−19.2%). The substantial decrease in winter precipitation leads to a slightly decreased annual mean precipitation in the SH LMR.

Over the land monsoon region, the projected onset of the rainy season is later and withdrawal is earlier than in the entire (both ocean and land) monsoon region (Tables 2 and 3) because of the oceanic monsoon onsets earlier and retreats later than those over the land. The projected onset of the NH land monsoon rainy season is unchanged, but the withdrawal date slightly delays by about 2–3 days, so the summer monsoon rainy season is slightly lengthened (Table 3). The projected SH land monsoon onset is delayed by 5–10 days, while the withdrawal date shows no change. The delayed NH land monsoon withdrawal and the delayed SH land monsoon onset dates are physically consistent, and the unchanged NH land monsoon

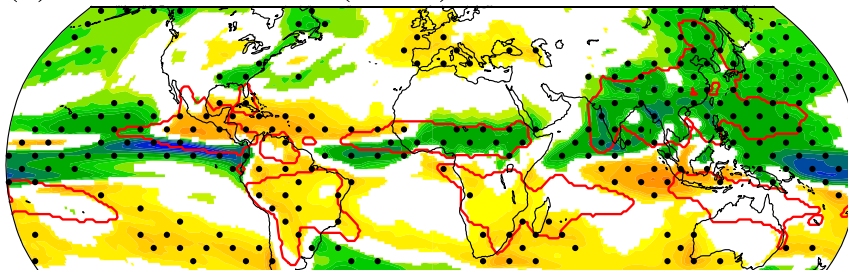
onset and SH land monsoon withdrawal are also consistent.

c. Global monsoon domain and annual range

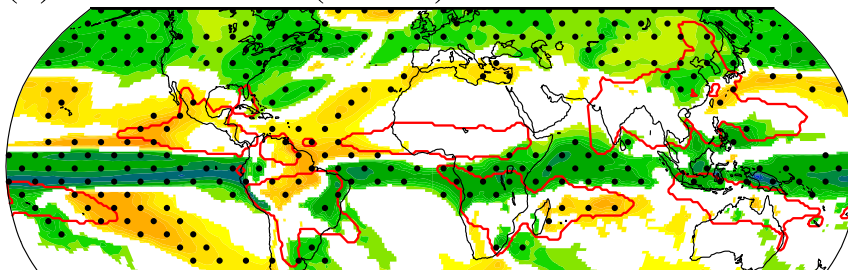
The projected total area of the GMP domain expands by 6.1%, primarily over the ocean (8.1%) (Fig. 6a). The land monsoon domain slightly increases by about 3.9%. The global dry regions decrease by about 5.2%. The continental boundary of the monsoon domain primarily follows the contour of the local summer (MJJAS in the NH) precipitation of 300 mm (Wang and LinHo 2002). The increase in summer monsoon precipitation would push the boundary farther inland, so the monsoon domain expands and the dry regions shrink correspondingly. The CMIP5 models' B4MME projected a 10.6% increase of the Asian land monsoon domain, while the CMIP6 15 MME projects an increase of about 6.0%.

The projected GMP intensity measured by the annual range of precipitation increases in northern African and Asia–western Pacific monsoons but decreases over Mexico and the adjacent oceans (Fig. 6b). In the SH, the projected increases of the annual ranges are over Indonesia, equatorial southern Africa, and southeast Brazil.

(a) Boreal summer (JJAS)



(b) Boreal winter (DJFM)



(c) Annual mean

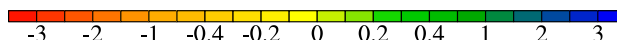
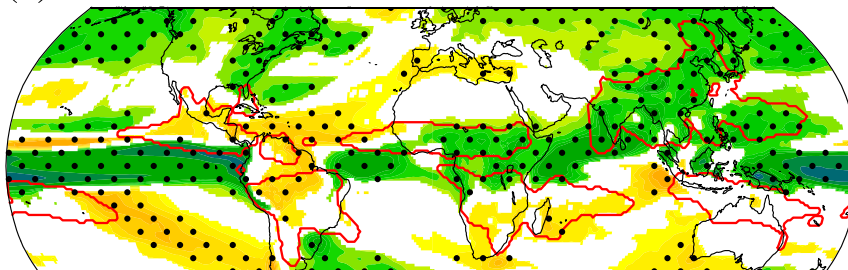


FIG. 7. Future changes in the climatological mean (a) boreal summer (JJAS), (b) boreal winter (DJFM), and (c) annual mean precipitation rates (mm day^{-1}). Changes are measured by the SSP2–4.5 (2065–2100) relative to historical simulation (1979–2014) in the 15 models' MME. The color-shaded region denotes where the changes are statistically significant at the 66% confidence level. Stippling denotes areas where the significance exceeds 95% confidence level by a Student's t test.

d. The patterns of GM precipitation change

During boreal summer (JJAS), the projected monsoon precipitation significantly increases over the Asian–western North Pacific and northern African monsoon regions, while it decreases over the North American monsoon region (Fig. 7a). The SH winter monsoon precipitation tends to be significantly reduced over Indonesia, implying an increased threat from wildfire during its dry season.

During austral summer (DJFM), the increased monsoon precipitation over Indonesia, equatorial southern Africa, and eastern Brazil is likely associated with the

projected equatorial warming pattern (Fig. 7b), because the rainfall in these regions is sensitive to the east–west shift of the Walker circulation, which is driven by zonal gradients of SST.

The future change of annual mean monsoon precipitation (Fig. 7c) features an NH–SH asymmetry and an east–west asymmetry in the NHM. The NHM rainfall increases mainly over Asia–western Pacific and northern Africa, while the SHM rainfall tends to reduce mainly in South America and southern Africa. The east–west asymmetry in NH is seen between enhanced Asian–African monsoon precipitation and reduced North American monsoon rainfall.

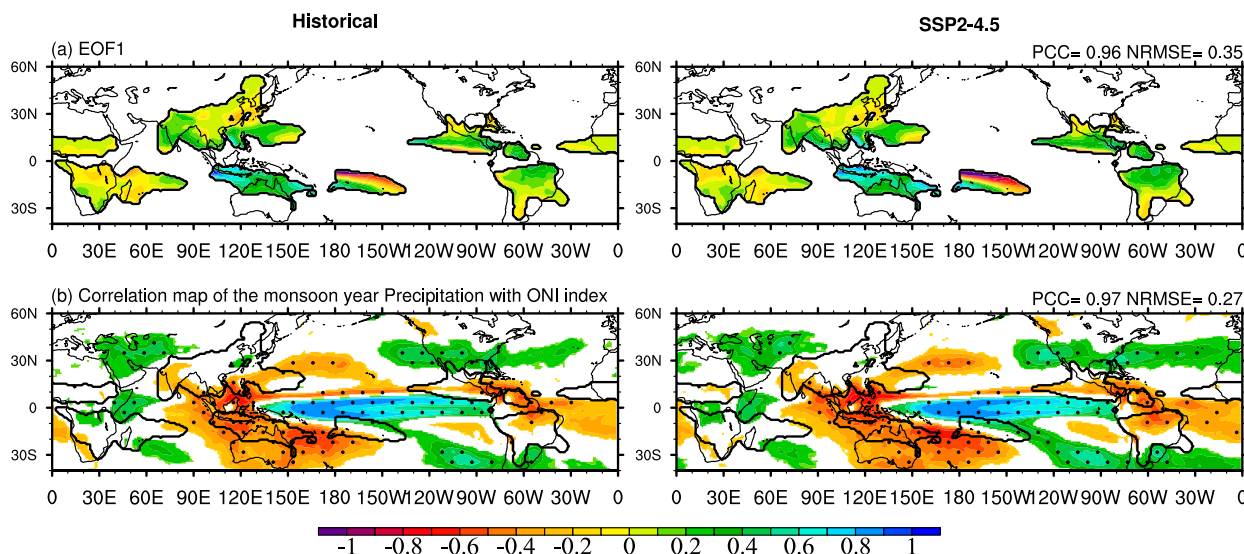


FIG. 8. Future changes in the interannual variability of the GMP and GM-ENSO relationship: (a) Spatial patterns of the leading EOF modes of the monsoon year mean GM precipitation in (left) the historical simulation and (right) the CMIP6 SSP2-4.5 run projected by 15 models' MME. For a fair comparison, the corresponding principal component has been normalized by its own standard deviation. (b) Correlation maps of the monsoon year mean precipitation (May to next April) with reference to the simultaneous ONI index simulated in (left) the historical run and (right) the SSP2-4.5 run. Only the CCs significant with $p < 0.34$ are plotted. The dotted region shows that CCs are significant with $p < 0.05$.

e. The leading mode of interannual variability and the GM-ENSO relationship

The spatial pattern of the leading mode in the SSP2-4.5 is exceptionally similar to that in historical simulation with $PCC = 0.96$ (Fig. 8a). However, the corresponding principal component is negatively correlated with simultaneous Niño-3.4 SST anomalies with a $CC = -0.64$ in the historical run (1979–2014) and $CC = -0.83$ ($n = 34$; $p < 0.01$) in the future projection (2065–2100), indicating that the leading mode will be more strongly controlled by ENSO variability, which may imply an enhanced GM predictability in future. Figure 8b shows that the present-day and future correlation maps of the monsoon-year GMP anomalies with respect to the Niño-3.4 SST anomalies are very similar ($CC = 0.97$). However, the absolute values of correlation coefficients tend to increase over Australian and American monsoon regions, indicating an enhanced relationship between ENSO and Australian and American monsoon regions.

f. The sensitivity of the monsoon precipitation to global warming

Figure 9 shows the time evolution of precipitation and surface air temperature (SAT) over the globe, NH, and SH simulated for 1979–2014 and projected from 2015 to 2100. The observed and simulated NHM precipitation trends are consistent during 1979–2014, which seems

encouraging and adds fidelity to the models' capability. The observed SHMP shows a large decadal fluctuation without an evident trend. The projected mean GMP increases from 4.26 (1979–2014) to 4.36 mm day⁻¹ (2065–2100), a moderate 2.3% increase, or 1% °C⁻¹. The NHM mean precipitation increases by 5.1% or 2.1% °C⁻¹. On the other hand, the SHM mean precipitation slightly decreases by 0.7% or 0.3% °C⁻¹. The models' spread as measured by one standard deviation is smaller than the trend, implying that the GMP and NHMP likely increase.

The projected global mean LMR increases from 3.75 (1979–2014) to 3.85 mm day⁻¹ (2065–2100), a moderate 2.7% increase, or 1.1% °C⁻¹ (Fig. 9). The projected NH LMR, however, increases by 2.8% °C⁻¹, which is faster than the total NHM precipitation. On the other hand, the SH LMR slightly decreases by 0.3% °C⁻¹, which is insignificant, given large intermodel spread.

g. NH and SH summer monsoon circulation

The intensities of the NH and SH monsoon circulations are defined by three indices shown in Table 4. The divergent wind index reflects the strength of the cross-equatorial meridional circulation averaged over the global monsoon longitudinal domain (10°–160°E, 100°–60°W). The projected NH summer monsoon circulation index and divergent wind index both decrease slightly (Table 4), but the decreases are not significant as they

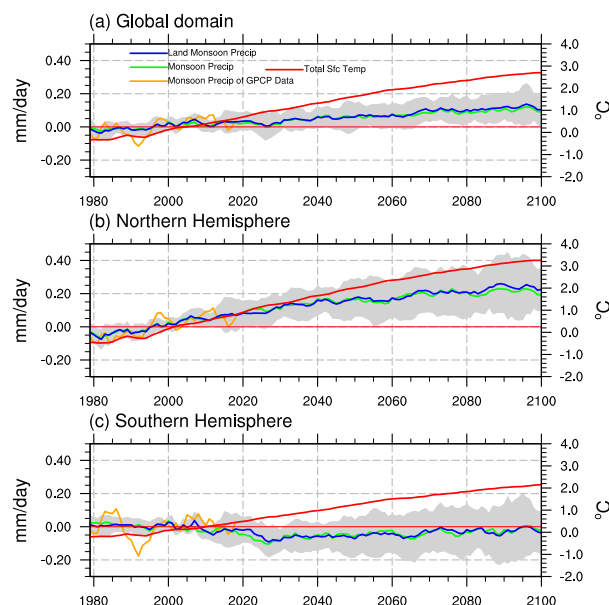


FIG. 9. Transient responses of the monsoon mean precipitation rate (green) and land monsoon mean precipitation rate (blue) vs global mean SAT (red) averaged over the (a) global, (b) NH, and (c) SH monsoon precipitation domains obtained from the 15MME for the historical run period (1850–2014) and the SSP2–4.5 run period (2015–2100). The MME’s uncertainty for mean monsoon precipitation was measured by 1 standard deviation of the individual models’ departures from the MME. A 5-yr moving averaging was applied to all time series to reduce the interannual variability.

are smaller than the one standard deviation of the models’ spread. However, the projected divergent wind index associated with the SH summer monsoon shows a significant decrease. The moderate weakening of the NH monsoon circulation suggests that while the enhanced NH summer monsoon precipitation tends to strengthen the monsoon circulation, the increased atmospheric static stability by top-heavy GHGs radiative heating tends to be dominant in reducing the circulation. The significant weakening of the SH summer monsoon circulation is consistent with

the slight decrease of the SH summer precipitation and significantly increased static stability. Since the monsoon meridional circulation occupies 190° of longitude, the weakening of monsoon meridional circulation has an important implication for the future change of Hadley circulation.

5. Causes of the future change of GM precipitation

Moisture budget analysis suggests that an increase in atmospheric moisture (thermodynamic effects) contributes positively to future precipitation changes, while a general weakening of the monsoon circulation (dynamic effects) acts to offset the positive thermodynamic effects partly. The temperature-driven increases in atmospheric specific humidity represent a robust moisture influence across climate models (Held and Soden 2006). However, the pattern of humidity change does not follow the temperature change pattern (Figs. 10a,b), suggesting that the increased specific humidity is not a direct result of local thermodynamic effects. The increased humidity varies strongly with season and locations (Figs. 10b,e). Local summer monsoon regions and equatorial regions show significant increases in specific humidity, while the climatological dry regions tend to have moderate increases. This non-uniform pattern suggests that the change of specific humidity is strongly regulated by the climatological mean monsoon circulation and the projected equatorial warming. The modulation by climatological circulation tends to yield a “wet-get-wetter” pattern (Held and Soden 2006), and the modulation by projected equatorial warming tends to favor a “warmer-get-wetter” pattern (Huang et al. 2013). In this sense, the specific humidity (thermodynamic effect) change involves the influence of the circulation (dynamic processes).

While the specific humidity increases are nearly uniform in summer monsoon regions (Figs. 10b,e), the spatial pattern of monsoon rainfall changes (Fig. 7) is

TABLE 4. Changes of the NH and SH summer monsoon circulation. The first row shows the NH summer monsoon circulation index defined by JJAS mean vertical shear of zonal winds (850 hPa minus 200 hPa) averaged over 0° – 20° N, 120° W– 120° E (Wang et al. 2013). The middle row has NH summer monsoon divergent circulation index measured by JJAS mean vertical shear of cross-equatorial meridional winds (850 hPa minus 200 hPa) averaged over 5° S– 5° N and monsoon longitudes (10° – 160° E, 100° – 60° W). The bottom row gives SH summer monsoon divergent wind index defined by DJFM mean vertical shear of cross-equatorial meridional winds (850 hPa minus 200 hPa) averaged over 5° S– 5° N and 10° – 160° E and 100° – 60° W. The units are meters per second, and the values in the parentheses are 1 standard deviation of the 15 models’ spread. The positive sign of the divergent wind index means a northward low-level flow in the NH summer monsoon and a southward low-level flow of the SH summer monsoon.

	Present day (1979–2014)	Future (2065–99)	Changes
NH summer monsoon circulation index	5.93	5.23	–0.70 (1.30)
NH summer monsoon divergent wind index	6.46	6.33	–0.13 (0.22)
SH summer monsoon divergent wind index	5.46	4.94	–0.52 (0.27)

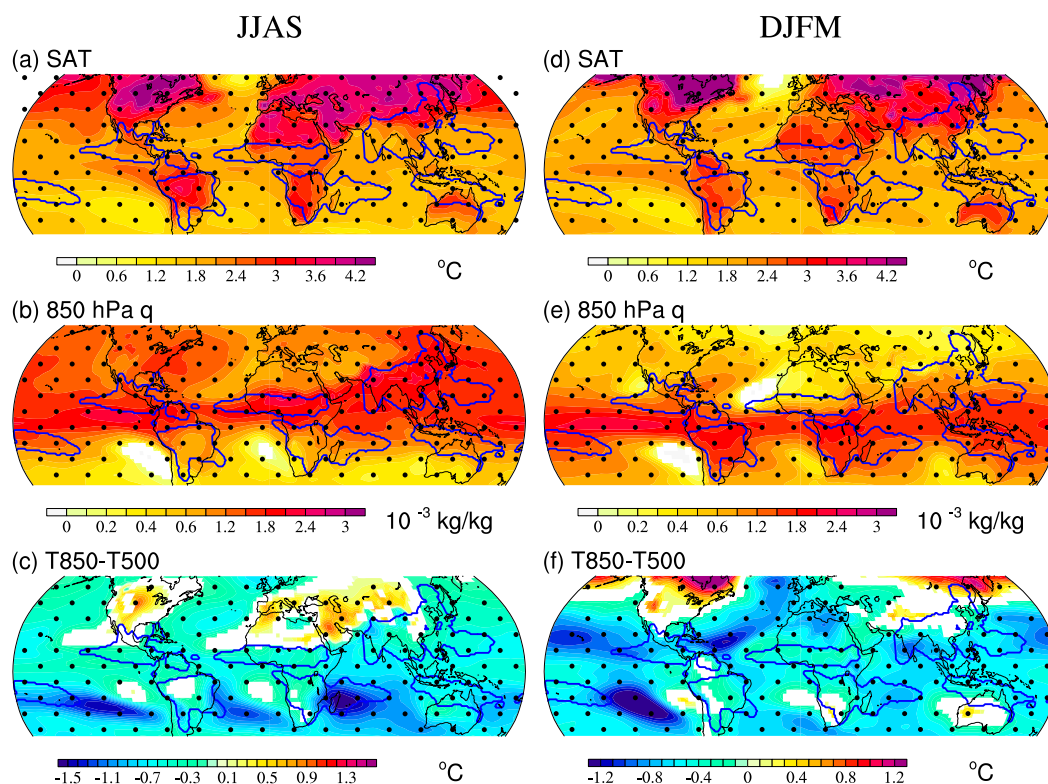


FIG. 10. Changes in thermodynamic fields, showing changes in (left) JJAS and (right) DJFM mean surface (a),(d) air temperature, (b),(e) 850-hPa specific humidity, and (c),(f) atmospheric static stability at the lower troposphere measured by the temperature difference between 850 and 500 hPa ($T_{850} - T_{500}$).

different from that of humidity change. Regardless of the substantial specific humidity increases during JJAS over the North American monsoon region, the precipitation there is reduced significantly. Similarly, many areas of SH monsoon show reduced precipitation despite the increased humidity. These facts indicate that the GHGs-induced circulation change must play a vital role in determining the spatial pattern and intensity of future monsoon precipitation change. In the literature, this dynamic effect has been relatively poorly understood, and its role is often underestimated.

The nonuniform warming-induced circulation changes are instrumental in explaining the future change of GM rainfall patterns and intensity. The GHGs' radiative forcing induces inhomogeneous thermal structure in both the horizontal and vertical directions. The vertically differential radiative forcing (top heavy) results in a warmer upper troposphere compared to the lower troposphere, which increases atmospheric static stability (Fig. 10c) and suppresses upward motion, providing a negative effect on precipitation intensity change nearly everywhere in monsoon regions. The horizontally differential warming, on the other hand, results in a robust "NH-warmer-than-SH" pattern, and "land-warmer-than-ocean" pattern (Fig. 10a), as well as a relatively

warmer equatorial ocean, especially in the eastern equatorial Pacific (with less intermodel agreement). Arguably, the NH-warmer-than-SH pattern favors a "wetter NHM and drier SHM" pattern in general, as shown in Fig. 7c. To support this argument, we examine each of the 15 models' future projections. Figure 11a shows that the models-projected NH summer monsoon precipitation increases are significantly related to the model projected interhemispheric temperature contrast change. This result suggests that the NH-warmer-than-SH pattern induced by GHG radiative forcing raises the sea level pressure in the SH compared with that in the NH, generating northward cross-equatorial flows and associated moisture and energy transport (Fig. 11b), thereby enhancing the NH summer monsoon rainfall.

It is conceivable that the land-warmer-than-ocean pattern may contribute to increased NH monsoon precipitation as the relative warming over continents may lead to enhanced land low pressure systems that drive low-level moist flows. To test this hypothesis, we have examined the relationship between the future changes of the Asian–northern African (Asian–NAF) summer monsoon precipitation and the land–ocean thermal contrast projected by 15 CMIP6 models under the SSP2–4.5. As shown in Fig. 12a, the changes of Asian–NAF

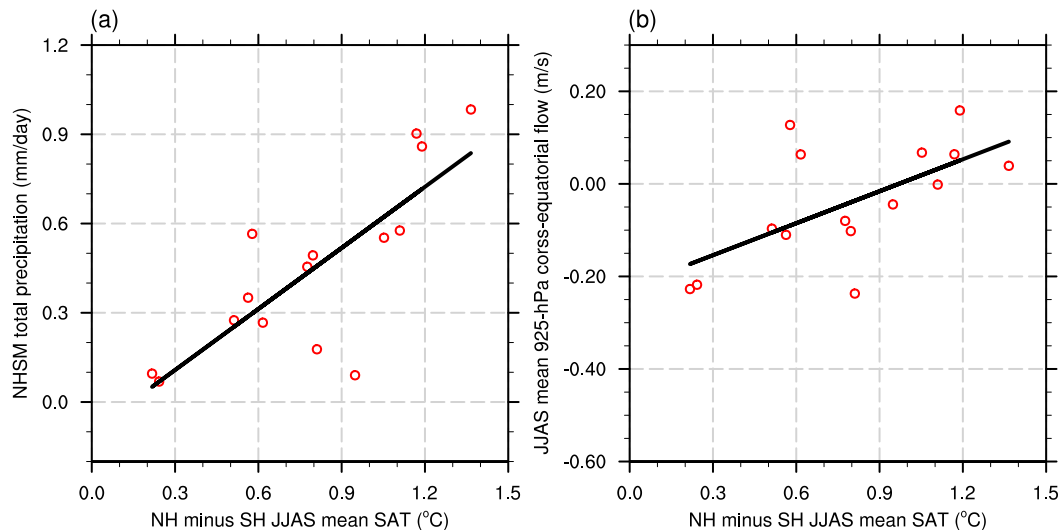


FIG. 11. Scatter diagrams showing the relationship between the future changes in the NH warmer-than-SH pattern and the NH summer monsoon precipitation projected by the 15 individual CMIP6 models under the SSP2-4.5 scenario: (a) The change of the total NH summer (JJAS) monsoon precipitation rate and (b) the change of the zonal mean (5°S–10°N) JJAS mean 925-hPa cross-equatorial flow as functions of the JJAS NH minus SH surface air temperature change (T2m for 40°S–0°, 0°–360°E – T2m for 40°S–0°, 0°–360°E). The correlation coefficients are 0.79 ($p < 0.01$) in (a) and 0.62 ($p < 0.01$) in (b).

summer monsoon precipitation are significantly correlated with the land–ocean thermal contrast that is measured by the land-minus-ocean surface air temperature with a correlation coefficient $r = 0.67$ ($p < 0.01$). The results suggest that the models that project a larger

change in the land–ocean thermal contrast predict a stronger Asian-NAF summer monsoon precipitation. Figure 12b further shows that the Asian-NAF summer monsoon rainfall changes are highly correlated to the land–ocean sea level pressure (SLP) differences with

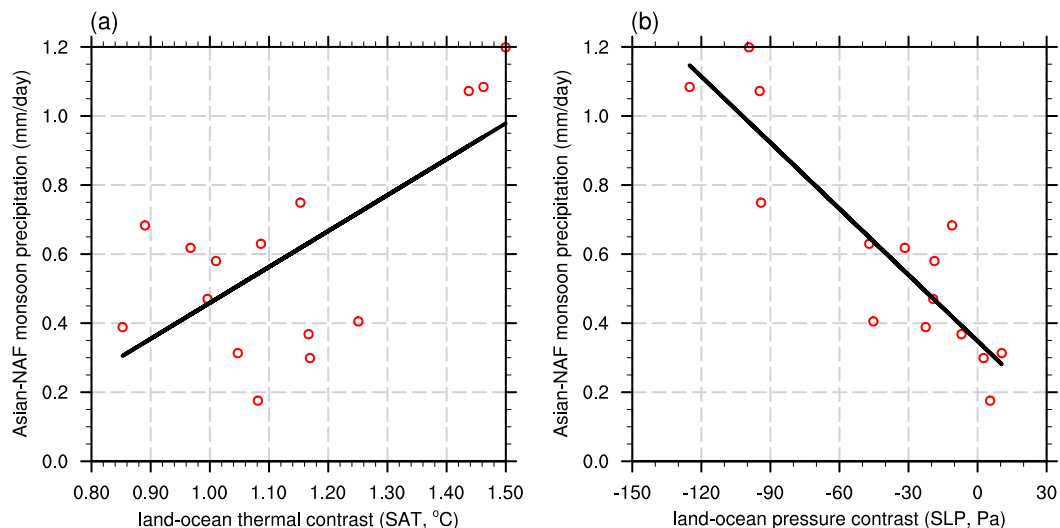


FIG. 12. Scatter diagrams showing the relationships between the future changes of the Asian–northern African (Asian-NAF) summer (JJAS) monsoon precipitation and the changes in (a) the land–ocean thermal contrast and (b) the land–ocean pressure contrast projected by 15 individual CMIP6 models under the SSP2-4.5 scenario. The land region denotes the land area within the domain 0°–50°N, 30°W–180°. The adjacent ocean regions include the western Pacific Ocean, northern Indian Ocean, and eastern Atlantic Ocean located in the domain 20°S–50°N, 30°W–180°. The land–sea thermal contrast is measured by the land-minus-ocean SAT, and the land–ocean pressure contrast is measured by the land minus ocean SLP. The correlation coefficients are 0.67 ($p < 0.01$) in (a) and -0.89 ($p < 0.01$) in (b).

$r = -0.89$ ($p < 0.01$). Physically, the land-warmer-than-ocean pattern generates a land-lower-than-ocean SLP field, enhancing the monsoon circulation and moisture convergence, increasing the monsoon precipitation. The CO_2 -induced enhancement of the land–sea thermal contrast and the resultant circulation changes are the most influential in the South Asian monsoon, which suggests an important role of the land warming on the Asian monsoon response to global warming (Endo et al. 2018).

Over the SH, the effect of the projected increasing local land–ocean thermal contrast is largely offset by the opposing remote effects of the NH-warmer-than-SH pattern, which contributes to the insignificant change in the SH monsoon precipitation.

A peculiar feature of GMP response to GHG forcing is the east–west asymmetry in the NH (increased Asian–African monsoon rainfall versus decreased North American monsoon rainfall; Fig. 7c). We note that the projected SST change features an El Niño-like eastern Pacific warming and relative cooling in the subtropical North Atlantic (Fig. 10a). We argue that this projected SST warming pattern may largely account for the drying North American monsoon in future. Figure 13 shows that models projecting relative warming in the equatorial eastern Pacific (5°S – 5°N , 120° – 80°W) compared to the tropical North Atlantic (10° – 20°N , 60° – 15°W) show more significant future decreases in the North American monsoon rainfall. Physically, the El Niño-like eastern Pacific warming may shift the ITCZ and monsoon convergence zone equatorward, causing reduced precipitation over large areas of central and North American monsoon regions, including Mexico and Central America, and the adjacent oceans. Over the eastern NH, pronounced warming over Eurasia and northern Africa continent (Fig. 10a) generates a large low pressure system, enhancing the climatological cyclonic monsoon circulation and transporting moisture to the African and Asian monsoon precipitation domain (Fig. 12).

6. Summary

The CMIP6 models' performance in simulation of the present-day solstice season precipitation climatology and GMP domain and intensity have been improved over the CMIP5 models. The CMIP6 models reproduce very well the solstice season mean precipitation pattern and the annual cycle (onset, peak, and withdrawal) of the NH monsoon, as well as realistic leading mode of interannual variability of GM and its relationship with ENSO. However, the models have severe common biases: 1) Significant precipitation errors are found in the equatorial (Pacific, Indian, and Atlantic) oceans,

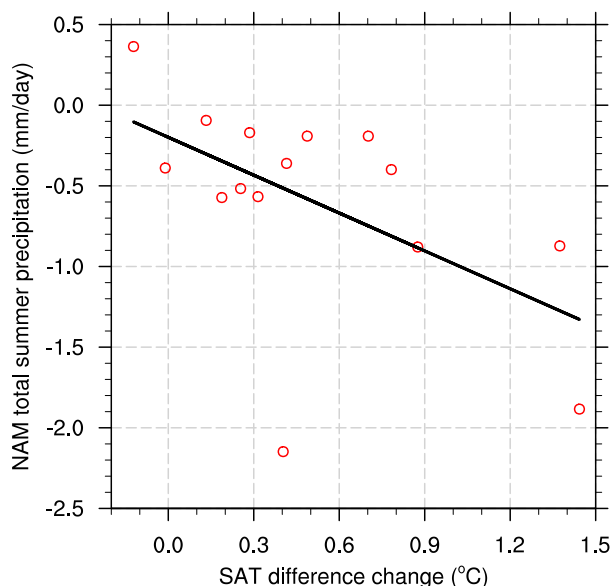


FIG. 13. Scatter diagram showing the relationship between the North American monsoon JJAS precipitation and the surface air temperature difference between the equatorial eastern Pacific (5°S – 5°N , 120° – 80°W) and the tropical Atlantic (10° – 20°N , 60° – 15°W) projected by the 15 CMIP6 models. The correlation coefficients are -0.55 ($p < 0.05$). A higher equatorial eastern Pacific SAT corresponds to a drier North American monsoon summer.

which link to the errors in the projected SST fields and link to the dry biases in the NH land monsoon regions and wet biases in NH oceanic monsoon region. 2) The models' MME overproduced annual mean precipitation in the SHM region by more than 20%, and the simulated onset is earlier by two pentads while the withdrawal is too late by 4–5 pentads (Table 1a). 3) The simulated oceanic monsoon domains extend excessively into the middle areas of the oceans. These biases, along with deficiencies in model cumulus parameterization, are one of the primary sources of uncertainties in projected monsoon changes.

Despite the above, the main features of future changes in GM rainfall under the SSP2–4.5 scenario can be summarized as follows.

- 1) The projected total NH land monsoon precipitation significantly increases by about $2.8\% \text{ } ^\circ\text{C}^{-1}$, which contrasts the insignificant decrease in the SH ($-0.3\% \text{ } ^\circ\text{C}^{-1}$) (Fig. 9). The overall change of GMP features a robust NH–SH asymmetry and an east–west asymmetry in the NH between enhanced Asian–African monsoons and a weakened North American monsoon (Fig. 7).
- 2) The NH monsoon rainy season as a whole may be lengthened by about 10 days because of delayed withdrawal, whereas the SH monsoon rainy season

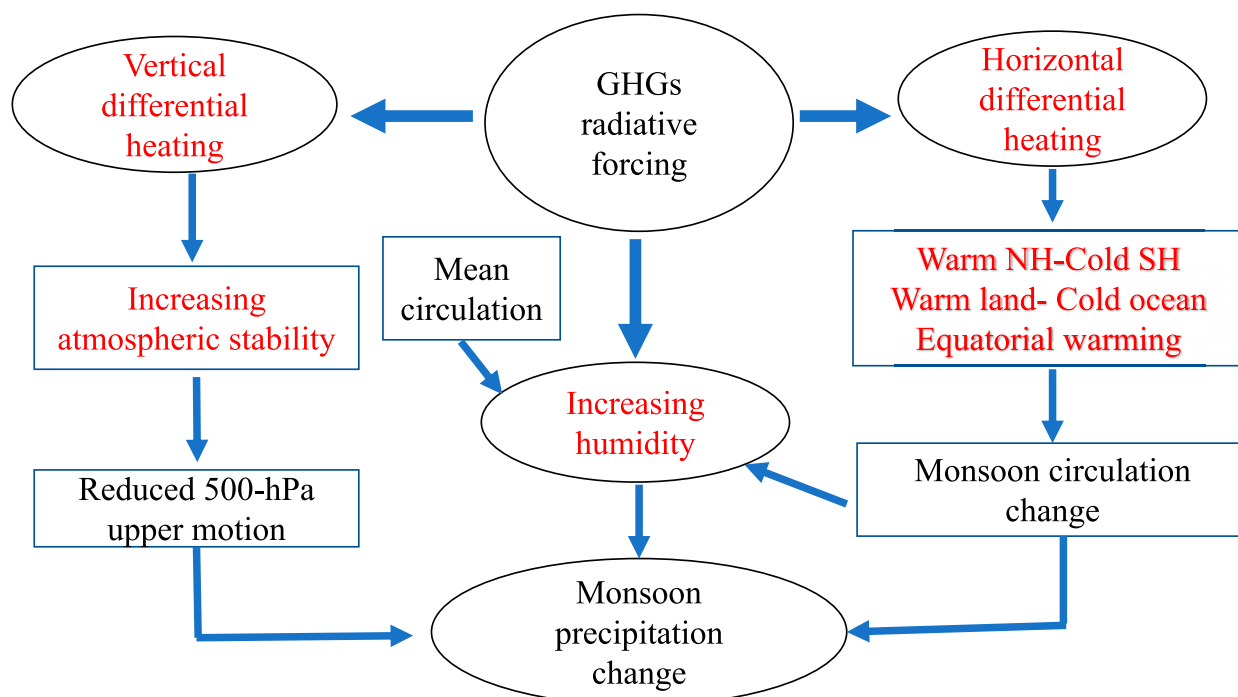


FIG. 14. Schematic diagram showing the processes by which the GHG radiative forcing controls GM change.

as a whole may be shortened by about 5 days because of delayed onset (Table 2).

- 3) The projected annual range of land monsoon rainfall as a whole increases by about 6.1% in the NH and by about 6.5% in the SH (Fig. 3 and Table 3) with summer wetter and winter drier. The increased annual range of NHM is primarily due to increased summer precipitation, while the increased annual range in SHM is attributed to both increased summer and decreased winter rainfall. This change increases the probability of summer floods and winter dryness.
- 4) The projected leading mode of GM interannual variability will be more strongly controlled by ENSO variability, implying an enhanced GM predictability in the future.
- 5) The projected total area of the GMP domain expands moderately by 6.1%, primarily over the ocean (8.1%), while the land monsoon domain slightly increases by about 3.9% (Fig. 6a). The global dry regions decrease by about 5.2% accordingly.
- 6) The projected NH summer monsoon circulation shows an insignificant decrease (Table 4). However, the cross-equatorially meridional circulations associated with the SH summer monsoon divergent circulations show significant decrease, which suggests the prevailing effects of the increased atmospheric static stability induced by the top-heavy GHGs radiative heating.

The major processes by which the GHG radiative forcing determines the GM future change is summarized in Fig. 14. The future change of GMP is attributed to the increased specific humidity and circulation changes. The GHG warming-induced specific humidity increase is not a local temperature-driven thermodynamic effect; rather, it is regulated by the climatological mean circulation and the projected tropical SST warming pattern. Note that the specific humidity increase is nearly uniform in all summer monsoon regions, but the precipitation changes vary considerably from region to region. The dynamic processes must play a crucial role in shaping the spatial pattern of the GM precipitation responses. The GHG-induced horizontally differential warming results in robust “NH-warmer than-SH” and “land-warmer-than-ocean” patterns, as well as an El Niño-like warming. The enhanced NH–SH thermal contrast favors for increasing NHM rainfall and reducing SHM rainfall (Fig. 11). The enhanced land–ocean thermal contrast between the vast Eurasian-African landmass and adjacent oceans favors enhanced Asian monsoon low pressure and increased monsoon rainfall over the Asian–northern African monsoon regions (Fig. 12). The projected eastern Pacific warming favors reducing the North American monsoon (Fig. 13) and Amazonian rainfall. The GHG-induced top-heavy heating stabilizes the atmosphere and suppresses ascent, partially offsetting the impact of increasing humidity on precipitation intensity.

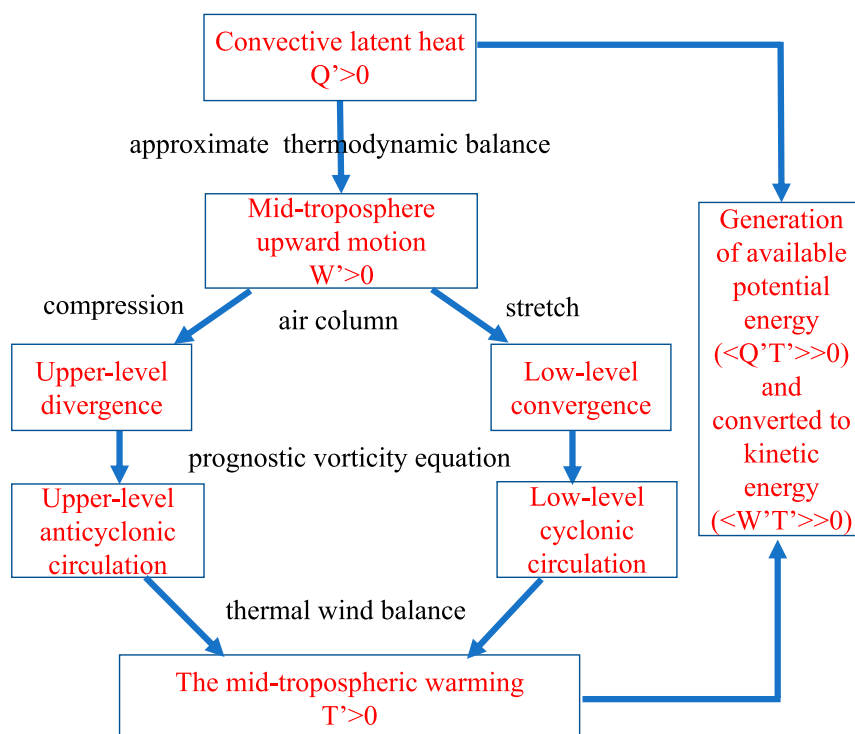


FIG. 15. Schematic diagram showing how the convective latent heat drives monsoon circulation. Angle brackets denote covariance.

Note that the CMIP6 projections for the global monsoon change generally agree with the CMIP5 results (Lee and Wang 2014). However, there are several differences: 1) The NH summer monsoon precipitation increases by $2.1\% \text{ }^{\circ}\text{C}^{-1}$ in CMIP6 MME, which is significantly lower than the CMIP5 B5MME projection ($3.1\% \text{ }^{\circ}\text{C}^{-1}$). 2) The overall onset of the NH summer monsoon has no appreciable change in CMIP6, while CMIP5 models suggest advanced onset. 3) In CMIP6 projection, the northern African wetting is stronger, and the Venezuela monsoon drying is weaker than the CMIP5 projections. Over northern and southeastern Australia, the CMIP5 model projected increased rainfall while CMIP6 projects no change. 4) The change in the land monsoon domain in CMIP6 is smaller than the CMIP5 models' assessment.

The interpretation here involves the idea that latent heat release drives tropical circulations, which has been challenged in recent decades. In a region of convection, the diabatic heating due mostly to latent heat release is approximately balanced by adiabatic cooling associated with ascent (Sobel and Bretherton 2000). It has been argued that this balance does not imply that the latent heat release is causing the adiabatic ascent. Note that this thermodynamic balance implies that convective heating does not directly drive temperature change in the tropics. However, that does not imply that convective heating cannot drive the tropical atmospheric

motion. As illustrated in Fig. 15, the midtropospheric ascent causes vortex shrinking (thus divergence) in the upper troposphere and vortex stretching (convergence) in the lower troposphere. The prognostic vorticity equation then predicts the divergent motion drives upper-level anticyclonic and low-level cyclonic circulations. This idea was first elaborated by Hoskins (1987) and demonstrated by many others (e.g., Sardeshmukh and Hoskins 1988). The midtropospheric temperature is then determined by thermal wind balance with the wind field determined from the vorticity equation. Thus, a positive temperature anomaly occurs in the convective region. From the energetics point of view, the generation of available potential energy (APE) requires the atmosphere warming up in the region of diabatic heating. Thus, in the convective region, the positive temperature anomaly and latent heating release make APE, which can then be converted to kinetic energy. In this sense, the convective latent heating plays a critical role in driving monsoon through the generation of the ascending motion. This large-scale perspective is useful in understanding the thermodynamic and dynamic structure of the monsoon and large-scale tropical circulation.

The projection uncertainty in the far future comes mainly from model and assumed scenario. Model uncertainty is mainly from circulation changes, which are primarily related to the uncertainties associated with

projected SST warming and land–sea thermal contrast (Shaw and Voigt 2015; Chen and Zhou 2015; Pascale et al. 2017). The results shown in Figs. 11 and 12 suggest that the uncertainty (intermodal spread) of the projected NH monsoon precipitation is significantly related to the models' projected NH–SH thermal contrast and the land–ocean thermal contrast. The results shown in Fig. 13 indicate that the uncertainty of projected North American monsoon precipitation is closely related to the models' projected SST warming in the equatorial eastern Pacific. Uncertainty in projected surface warming patterns is closely related to present-day model biases, including the cold-tongue bias in the tropical eastern Pacific and a cold bias in marine stratocumulus cloud regions (Nam et al. 2012; Chen and Zhou 2015; Li et al. 2016; Ying et al. 2019). Monsoons are strongly influenced by cloud and water vapor feedbacks (Jalihal et al. 2019; Byrne and Zanna 2019, manuscript submitted to *J. Climate*), yet how the significant variations in these feedbacks across climate models impact monsoon uncertainties is unknown. The extent to which the models' shortcomings contribute to the uncertainty of future monsoon rainfall projections deserves in-depth studies.

Acknowledgments. The authors appreciate three reviewers' constructive comments on an earlier version of the paper, which lead to an improved presentation. The first author thanks Prof. Brian Hoskins for helpful e-mail discussion. This work was supported by the National Natural Science Foundation of China (Grants 41420104002, and 41971108). Authors Liu and Wang are supported by the National Key Research and Development Program of China (Grant 2016YFA0600401). Wang acknowledges the support of NSF/Climate Dynamics Award AGS-1540783. Author Jin acknowledges the support from the program of China Scholarships Council (201806860029). This is Publication Number 10981 of the School of Ocean and Earth Science and Technology, Publication Number 1445 of the International Pacific Research Center, and Publication Number 310 of the Earth System Modeling Center.

REFERENCES

- Adler, R. F., and Coauthors, 2003: The version-2 Global Precipitation Climatology Project (GPCP) monthly precipitation analysis (1979–present). *J. Hydrometeorol.*, **4**, 1147–1167, [https://doi.org/10.1175/1525-7541\(2003\)004<1147:TVGPCP>2.0.CO;2](https://doi.org/10.1175/1525-7541(2003)004<1147:TVGPCP>2.0.CO;2).
- Chang, C.-P., Z. Wang, J. McBride, and C.-H. Liu, 2005: Annual cycle of Southeast Asia–Maritime Continent rainfall and the asymmetric monsoon transition. *J. Climate*, **18**, 287–301, <https://doi.org/10.1175/JCLI-3257.1>.
- , M.-M. Lu, and H. Lim, 2016: Monsoon convection in the maritime continent: Interaction of large-scale motion and complex terrain. *Multiscale Convection-Coupled Systems in the Tropics: A Tribute to Dr. Michio Yanai*, Meteor. Monogr., No. 56, Amer. Meteor. Soc., 6.1–6.29, <https://doi.org/10.1175/AMSMONOGRAPHS-D-15-0011.1>.
- Chen, X., and T. Zhou, 2015: Distinct effects of global mean warming and regional sea surface warming pattern on projected uncertainty in the South Asian summer monsoon. *Geophys. Res. Lett.*, **42**, 9433–9439, <https://doi.org/10.1002/2015GL066384>.
- Christensen, J. H., and Coauthors, 2013: Climate phenomena and their relevance for future regional climate change. *Climate Change 2013: The Physical Science Basis*, T. F. Stocker et al., Eds., Cambridge University Press, 1217–1308.
- Endo, H., A. Kitoh, and H. Ueda, 2018: A unique feature of the Asian summer monsoon response to global warming: The role of different land–sea thermal contrast change between the lower and upper troposphere. *SOLA*, **14**, 57–63, <https://doi.org/10.2151/SOLA.2018-010>.
- Eyring, V., S. Bony, G. A. Meehl, C. A. Senior, B. Stevens, R. J. Stouffer, and K. E. Taylor, 2016: Overview of the Coupled Model Intercomparison Project Phase 6 (CMIP6) experimental design and organization. *Geosci. Model Dev.*, **9**, 1937–1958, <https://doi.org/10.5194/GMD-9-1937-2016>.
- Hann, J., 1908: *Handbuch der Klimatologie (Handbook of Climatology)*. Vol. 3, Engelhorn, 394 pp.
- Held, I. M., and B. J. Soden, 2006: Robust responses of the hydrological cycle to global warming. *J. Climate*, **19**, 5686–5699, <https://doi.org/10.1175/JCLI3990.1>.
- Hoskins, B. J., 1987: Diagnosis of forced and free variability in the atmosphere. *Atmospheric and Oceanic Variability*, H. Cattle, Eds., Royal Meteorological Society, 57–74.
- , 1996: On the existence and strength of the summer subtropical anticyclones. *Bull. Amer. Meteor. Soc.*, **77**, 1287–1292.
- , and B. Wang, 2006: Large-scale atmospheric dynamics. *The Asian Monsoon*, Springer, 357–415.
- Hsu, P., T. Li, H. Murakami, and A. Kitoh, 2013: Future change of the global monsoon revealed from 19 CMIP5 models. *J. Geophys. Res. Atmos.*, **118**, 1247–1260, <https://doi.org/10.1002/JGRD.50145>.
- Huang, B., and Coauthors, 2017: Extended reconstructed sea surface temperature, version 5 (ERSSTv5): Upgrades, validations, and intercomparisons. *J. Climate*, **30**, 8179–8205, <https://doi.org/10.1175/JCLI-D-16-0836.1>.
- Huang, P., S.-P. Xie, K. Hu, G. Huang, and R. Huang, 2013: Patterns of the seasonal response of tropical rainfall to global warming. *Nat. Geosci.*, **6**, 357–361, <https://doi.org/10.1038/ngeo1792>.
- Jalihal, C., J. Srinivasan, and A. Chakraborty, 2019: Modulation of Indian monsoon by water vapor and cloud feedback over the past 22,000 years. *Nat. Commun.*, **10**, 5701, <https://doi.org/10.1038/s41467-019-13754-6>.
- Joseph, P. V., K. P. Sooraj, and C. K. Rajan, 2006: The summer monsoon onset process over South Asia and an objective method for the date of monsoon onset over Kerala. *Int. J. Climatol.*, **26**, 1871–1893, <https://doi.org/10.1002/JOC.1340>.
- Khromov, S. P., 1957: Die geographische Verbreitung der Monsune (The geographical distribution of the monsoons). *Petermanns Geogr. Mitt.*, **101**, 234–237.
- Kitoh, A., H. Endo, K. Krishna Kumar, I. F. A. Cavalcanti, P. Goswami, and T. Zhou, 2013: Monsoons in a changing world: A regional perspective in a global context. *J. Geophys. Res. Atmos.*, **118**, 3053–3065, <https://doi.org/10.1002/JGRD.50258>.
- Lee, J.-Y., and B. Wang, 2014: Future change of global monsoon in the CMIP5. *Climate Dyn.*, **42**, 101–119, <https://doi.org/10.1007/s00382-012-1564-0>.

- Li, G., S.-P. Xie, Y. Du, and Y. Luo, 2016: Effects of excessive equatorial cold tongue bias on the projections of tropical Pacific climate change. Part I: The warming pattern in CMIP5 multi-model ensemble. *Climate Dyn.*, **47**, 3817–3831, <https://doi.org/10.1007/s00382-016-3043-5>.
- Nam, C., S. Bony, J.-L. Dufresne, and H. Chepfer, 2012: The ‘too few, too bright’ tropical low-cloud problem in CMIP5 models. *Geophys. Res. Lett.*, **39**, L21801, <https://doi.org/10.1029/2012GL053421>.
- O'Neill, B. C., and Coauthors, 2016: The Scenario Model Intercomparison Project (ScenarioMIP) for CMIP6. *Geosci. Model Dev.*, **9**, 3461–3482, <https://doi.org/10.5194/gmd-9-3461-2016>.
- Pascale, S., W. R. Boos, S. Bordoni, T. L. Delworth, S. B. Kapnick, H. Murakami, G. A. Vecchi, and W. Zhang, 2017: Weakening of the North American monsoon with global warming. *Nat. Climate Change*, **7**, 806–812, <https://doi.org/10.1038/nclimate3412>.
- Ramage, C. S., 1971: *Monsoon Meteorology*. International Geophysics Series, Vol. 15, Academic Press, 296 pp.
- Rayner, N. A. A., D. E. Parker, E. B. Horton, C. K. Folland, L. V. Alexander, D. P. Rowell, E. C. Kent, and A. Kaplan, 2003: Global analyses of sea surface temperature, sea ice, and night marine air temperature since the late nineteenth century. *J. Geophys. Res.*, **108**, 4407, <https://doi.org/10.1029/2002JD002670>.
- Rodwell, M. J., and B. J. Hoskins, 1996: Monsoons and the dynamics of deserts. *Quart. J. Roy. Meteor. Soc.*, **122**, 1385–1404, <https://doi.org/10.1002/qj.49712253408>.
- Sardeshmukh, P. D., and B. J. Hoskins, 1988: The generation of global rotational flow by steady idealized tropical divergence. *J. Atmos. Sci.*, **45**, 1228–1251, [https://doi.org/10.1175/1520-0469\(1988\)045<1228:TGOGRF>2.0.CO;2](https://doi.org/10.1175/1520-0469(1988)045<1228:TGOGRF>2.0.CO;2).
- Shaw, T. A., and A. Voigt, 2015: Tug of war on summertime circulation between radiative forcing and sea surface warming. *Nat. Geosci.*, **8**, 560–566, <https://doi.org/10.1038/ngeo2449>.
- Sobel, A. H., and C. S. Bretherton, 2000: Modeling tropical precipitation in a single column. *J. Climate*, **13**, 4378–4392, [https://doi.org/10.1175/1520-0442\(2000\)013<4378:MTPIAS>2.0.CO;2](https://doi.org/10.1175/1520-0442(2000)013<4378:MTPIAS>2.0.CO;2).
- Trenberth, K. E., D. P. Stepaniak, and J. M. Caron, 2000: The global monsoon as seen through the divergent atmospheric circulation. *J. Climate*, **13**, 3969–3993, [https://doi.org/10.1175/1520-0442\(2000\)013<3969:TGMAST>2.0.CO;2](https://doi.org/10.1175/1520-0442(2000)013<3969:TGMAST>2.0.CO;2).
- Wang, B., 1994: Climatic regimes of tropical convection and rainfall. *J. Climate*, **7**, 1109–1118, [https://doi.org/10.1175/1520-0442\(1994\)007<1109:CROTCA>2.0.CO;2](https://doi.org/10.1175/1520-0442(1994)007<1109:CROTCA>2.0.CO;2).
- , and LinHo, 2002: Rainy season of the Asian–Pacific summer monsoon. *J. Climate*, **15**, 386–398, [https://doi.org/10.1175/1520-0442\(2002\)015<0386:RSOTAP>2.0.CO;2](https://doi.org/10.1175/1520-0442(2002)015<0386:RSOTAP>2.0.CO;2).
- , and Q. Ding, 2006: Changes in global monsoon precipitation over the past 56 years. *Geophys. Res. Lett.*, **33**, L06711, <https://doi.org/10.1029/2005GL025347>.
- , and —, 2008: Global monsoon: Dominant mode of annual variation in the tropics. *Dyn. Atmos. Oceans*, **44**, 165–183, <https://doi.org/10.1016/j.dynatmoce.2007.05.002>.
- , —, and P. V. Joseph, 2009: Objective definition of the Indian summer monsoon onset. *J. Climate*, **22**, 3303–3316, <https://doi.org/10.1175/2008JCLI2675.1>.
- , —, —, and B. Xiang, 2013: Northern Hemisphere summer monsoon intensified by mega-El Niño/Southern Oscillation and Atlantic multidecadal oscillation. *Proc. Natl. Acad. Sci. USA*, **110**, 5347–5352, <https://doi.org/10.1073/pnas.1219405110>.
- , J. Li, and Q. He, 2017: Variable and robust East Asian monsoon rainfall response to El Niño over the past 60 years (1957–2016). *Adv. Atmos. Sci.*, **34**, 1235–1248, <https://doi.org/10.1007/s00376-017-7016-3>.
- , X. Luo, M.-Y. Yang, W. Sun, M. A. Cane, W. Cai, S.-W. Yeh, and J. Liu, 2019: Historical change of El Niño properties sheds light on future changes of extreme El Niño. *Proc. Natl. Acad. Sci. USA*, **116**, 22 512–22 517, <https://doi.org/10.1073/pnas.1911130116>.
- Wang, P. X., B. Wang, H. Cheng, J. Fasullo, Z. T. Guo, T. Kiefer, and Z. Y. Liu, 2014: The global monsoon across time scales: Is there coherent variability of regional monsoons? *Climate Past Discuss.*, **10**, 2163–2291, <https://doi.org/10.5194/cpd-10-2163-2014>.
- , —, —, —, Z. Guo, T. Kiefer, and Z. Liu, 2017: The global monsoon across time scales: Mechanisms and outstanding issues. *Earth-Sci. Rev.*, **174**, 84–121, <https://doi.org/10.1016/j.earscirev.2017.07.006>.
- Webster, P. J., 1987: The variable and interactive monsoon. *Monsoons*, J. S. Fein and P. L. Stephens, Eds., John Wiley and Sons, 269–330.
- Yasunari, T., 1991: The monsoon year—A new concept of the climatic year in the tropics. *Bull. Amer. Meteor. Soc.*, **72**, 1331–1338, [https://doi.org/10.1175/1520-0477\(1991\)072<1331:TMYNCO>2.0.CO;2](https://doi.org/10.1175/1520-0477(1991)072<1331:TMYNCO>2.0.CO;2).
- Ying, J., P. Huang, T. Lian, and H. Tan, 2019: Understanding the effect of an excessive cold tongue bias on projecting the tropical Pacific SST warming pattern in CMIP5 models. *Climate Dyn.*, **52**, 1805–1818, <https://doi.org/10.1007/s00382-018-4219-y>.
- Zhang, S., and B. Wang, 2008: Global summer monsoon rainy seasons. *Int. J. Climatol.*, **28**, 1563–1578, <https://doi.org/10.1002/JOC.1659>.
- Zhang, W., T. Zhou, L. Zhang, and L. Zou, 2019: Future intensification of the water cycle with an enhanced annual cycle over global land monsoon regions. *J. Climate*, **32**, 5437–5452, <https://doi.org/10.1175/JCLI-D-18-0628.1>.